

Article

Not peer-reviewed version

---

# Experimental and Numerical Analysis of the Quasi-Static and Dynamic Behavior of Silicate Materials

---

[Tomasz Jankowiak](#)<sup>\*</sup>, Jakub Rafał Ossowski, [Alexis Rusinek](#), Slim Bahi

Posted Date: 7 November 2024

doi: 10.20944/preprints202411.0507.v1

Keywords: silicate; quasi-static; impact; CDP model; modeling; experiments



Preprints.org is a free multidiscipline platform providing preprint service that is dedicated to making early versions of research outputs permanently available and citable. Preprints posted at Preprints.org appear in Web of Science, Crossref, Google Scholar, Scilit, Europe PMC.

Copyright: This is an open access article distributed under the Creative Commons Attribution License which permits unrestricted use, distribution, and reproduction in any medium, provided the original work is properly cited.

Article

# Experimental and Numerical Analysis of the Quasi-Static and Dynamic Behavior of Silicate Materials

Tomasz Jankowiak <sup>1,\*</sup>, Jakub Rafał Ossowski <sup>2</sup>, Alexis Rusinek <sup>3</sup> and Slim Bahi <sup>3</sup>

<sup>1</sup> Poznan University of Technology, Institute of Structural Analysis, Piotrowo 5, 60-965 Poznan, Poland

<sup>2</sup> Silikaty Szlachta S.C., Ceramiczna 25, 83-243 Szlachta, Poland

<sup>3</sup> Lorraine University, ENSAM-Arts et Métiers ParisTech, Laboratory of Microstructure Studies and Mechanics of Materials (LEM3), UMR CNRS 7239, 57078 Metz, France

\* Correspondence: tomasz.jankowiak@put.poznan.pl

**Abstract:** The study investigated both the static and dynamic behavior of silicate materials through a series of experimental and numerical tests. Compression tests were conducted on cubic samples, three-point bending tests on beams, and perforation tests on silicate plates. In the compression tests, stress-strain curves were generated, enabling the calibration of the Concrete Damaged Plasticity (CDP) model for silicate materials. The tensile strength of the silicate was assessed using three-point bending tests, while dynamic perforation tests determined the impact resistance of silicate when subjected to a rigid projectile. The perforation tests provided insight into the failure mechanisms of silicate plates under projectile impact at velocities approaching the ballistic limit. Additionally, the numerical simulations for all the experimental tests were performed using the Abaqus software, in order to validate the accuracy of the material behavior model and confirmed the appropriateness of the calibrated parameters for the chosen model. The results showed a strong qualitative and quantitative correlation with the experimental data, demonstrating the robustness of the adopted approach.

**Keywords:** silicate; quasi-static; impact; CDP model; modeling; experiments

## 1. Introduction

Silicate blocks, particularly calcium silicate, are widely recognized as robust and versatile building materials in modern construction. These blocks are formed through an autoclaving process that involves a mixture of sand, lime (calcium oxide or calcium hydroxide), and water. The key chemical reaction in this process is hydration, which leads to the formation of calcium silicate hydrate [1], a material known for its high strength and durability. The hydration process imparts silicate blocks with advantageous properties such as high compressive strength, thermal insulation, and fire resistance, making them a preferred choice for load-bearing walls, partition walls, and other structural elements in residential, commercial, and industrial construction.

Calcium silicate blocks exhibit a variety of structural forms, including solid blocks, hollow blocks, and perforated blocks [2], each serving distinct roles depending on the construction requirements. These blocks are typically installed using traditional masonry techniques with mortar or adhesive, and are often finished with plaster, paint, or external cladding materials [3,4]. Their composition and performance characteristics vary based on the specific manufacturing processes employed, yet they consistently demonstrate excellent resistance to moisture, pests, and decay, contributing to the longevity and integrity of the structures they are used in [5].

A notable advancement in the silicate block category is autoclaved aerated concrete (AAC) blocks, which are lightweight and offer enhanced thermal insulation properties [6]. The unique porous structure of AAC blocks significantly reduces the weight of the material while maintaining

sufficient strength for structural applications, thus providing both thermal and load-bearing advantages. These materials contribute to energy efficiency in buildings by improving insulation and reducing the need for active heating and cooling systems.

Research has shown that the mechanical performance of masonry made from calcium silicate blocks is influenced by factors such as joint thickness and mortar strength [7,8]. Studies reveal that thinner joints made with low-strength mortar significantly affect the mechanical properties of the masonry, while higher mortar strengths generally improve the overall structural performance. However, these studies often focus on the behavior of the walls as a whole rather than the mechanical properties of the individual blocks [9,10].

In contrast, this study aims to investigate the intrinsic mechanical properties of silicate blocks themselves, with a focus on compressive strength, tensile strength, and impact resistance. Unlike previous research, which predominantly examined static behaviors like compressive strength in wall assemblies, this study expands the scope to include both tensile strength and dynamic impact resistance of the individual blocks. This comprehensive mechanical analysis of silicate blocks is novel, combining experimental testing with numerical simulations to provide a holistic understanding of the material's performance under various loading conditions. Such insights are crucial for optimizing the use of silicate materials in construction, particularly in applications requiring enhanced resilience to both static and dynamic stresses.

This research contributes to filling a gap in the literature by offering new experimental data and simulations that address not only the compressive behavior but also the tensile and impact properties of silicate blocks, thus broadening the understanding of their potential in construction [11,12].

## 2. Experimental Analysis and Description of the Geometry Specimens

The laboratory tests were conducted at the laboratory of the Institute of Structural Analysis, Poznan University of Technology. Compression tests were performed to characterize the strength and stress-strain behavior of the silicate material investigated in this study. Two silicate blocks, marked by the manufacturer (Silikaty Szlachta S.C.) with the symbol N18A, were randomly selected from a single production batch [13]. The blocks were visually inspected for external defects, and their dimensions were carefully measured. The nominal dimensions of the blocks were 250x180x220 mm. The visual inspection and dimensional analysis were conducted in accordance with the PN-EN 771-2 standard [14], using calibrated measuring instruments.

Subsequently, cubic samples with nominal dimensions of 50x50x50 mm were cut from the blocks. The cutting process was performed using a circular concrete saw with a diamond blade, ensuring accurate angles and precise sample dimensions. After discarding any damaged samples, a total of 23 samples were obtained, from which 12 were randomly selected for testing (see Table 1). A typical cubic sample is shown in Figure 1a [15].

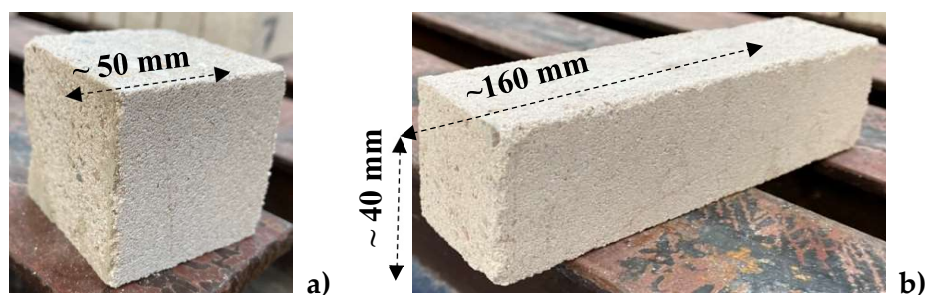




**Figure 1.** Selected silicate specimens for tests; a) compression, b) three-point bending, c) perforation.

**Table 1.** Dimensions of the selected compressive samples.

No. sample	Dimensions (mm)			Mass (g)
	L (length)	W (width)	H (height)	
1	50.1	50.0	50.6	246.0
2	50.5	50.9	50.5	248.2
3	51.2	50.3	51.1	257.2
4	50.6	50.4	50.8	245.8
5	50.9	50.5	50.8	247.8
6	51.2	51.1	51.1	270.8
7	50.5	50.2	50.8	250.0
8	51.0	51.3	51.2	279.6
9	50.4	50.5	51.0	259.0
10	50.2	50.2	50.0	245.8
11	51.1	51.0	50.8	243.0
12	51.0	50.5	50.8	243.0
Average values:	50.8	50.6	50.8	253.4

The preparation of the samples ensured that the dimensions were consistent, with minimal dispersion during the cutting process. Similarly, the mass of the samples showed limited variation. The dimensional measurements of the 23 specimens (length, width, and height) remained close to the nominal size of 50 mm, with average values of 50.8 mm, 50.6 mm, and 50.8 mm, respectively. Additionally, the average mass of the samples was 253.4 grams, indicating a well-controlled preparation process. These results confirm that the samples were prepared with high precision, allowing for reliable testing and analysis.

The three-point bending tests were conducted to evaluate the tensile behavior and strength of the silicate material. For this purpose, hollow elements marked by the manufacturer with the symbol N24PA, having nominal dimensions of 250x240x220 mm, were used to fabricate silicate beams with nominal dimensions of 40x40x160 mm. This element belongs to the same strength class as the previously used N18A block and was sourced from the same material batch. No cracks, chips, or other defects that could potentially affect the test results, were observed.

Rectangular samples were cut using the same method described previously. A total of 15 samples were prepared, of which 2 were rejected due to imperfections and damage. An exemplary sample is depicted in Figure 1b. From the remaining 13 samples, 8 were randomly selected for further dimensional and mass measurements, with the results presented in Table 2 [15].

**Table 2.** Dimensions of the selected three-point bending samples.

No. sample	Dimensions (mm)			Mass (g)
	L (length)	W (width)	H (height)	
1	164.0	42.0	41.0	533.8
2	161.0	41.0	42.0	534.2
3	161.0	42.0	41.0	534.2
4	161.0	42.0	41.0	529.6
5	161.0	41.0	42.0	551.0
6	161.0	41.0	42.0	571.2
7	161.0	43.0	41.0	551.6
8	162.0	41.0	41.0	527.2
Average values:	161.5	41.6	41.4	541.6

The perforation tests were conducted to assess the dynamic behavior of the silicate material. The samples were composed of sand-lime blocks marked by the manufacturer as N24PA, which share the same strength class and originate from the same material batch as the N18A elements used in the static compression tests. Rectangular plates with nominal dimensions of 120x120x30 mm were cut using the same methodology applied to the previous silicate samples. The appearance of a representative sample is shown in Figure 1c.

Following the cutting process, 10 samples were obtained; however, 3 were discarded due to minor damage, such as visible cracks. Each remaining sample was meticulously dimensioned, with the final measurements presented in Table 3. The final inspection of the visual condition of the silicate samples confirmed the absence of defects and cracks that could adversely impact the macroscopic results of the material tests. The average density of the silicate material was determined to be 1600 kg/m<sup>3</sup>.

**Table 3.** Dimensions of the selected impacted samples.

No. sample	Dimensions (mm)			Mass (g)
	L (length)	W (width)	T (thickness)	
1	121.5	121.0	33.0	901.2
2	121.8	126.0	32.0	904.6
3	121.6	121.0	34.0	910.1
4	121.0	121.0	34.0	907.8
5	127.1	122.0	34.5	924.2
6	121.0	121.0	32.0	913.8
7	122.0	121.0	35.0	921.2
Average values:	122.3	121.9	33.5	911.8

### 2.1. Definition of the Material Behavior Under Compression

An Instron hydraulic machine equipped with displacement control was used to conduct the compression tests on the silicate blocks, as shown in Figure 2a. During the experiments, the force, displacement, nominal stress, and strain were continuously recorded. The failure patterns were documented using a camera. Each test was terminated when the maximum force was reached and subsequently dropped by 40%. After attaining the maximum capacity, the samples were subjected to crushing. The maximum force  $F_{max}$  and compressive strength  $f_c$  for all samples are presented in Table 4, with the average compressive strength  $\bar{f}_c$  calculated to be 15.2 MPa.

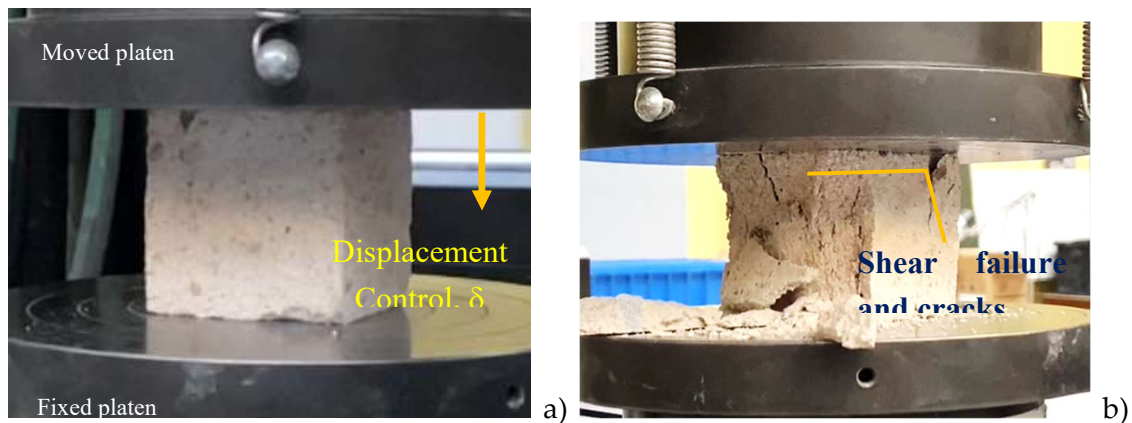


**Figure 2.** Experimental Compression Test: a) Sample Prior to Testing; b) Sample Post-Test Displaying Visible Fracture Mechanism.

**Table 4.** The compressive strength.

No. sample	Maximum force (N)	Compressive strength (MPa)
1	42823	17.1
2	36436	14.6
3	34062	13.6
4	39674	15.9
5	48951	19.6
6	36394	14.6
7	31309	12.2
8	37548	14.4
9	37315	14.7
10	39582	15.8
11	40706	15.6
12	38417	15.2
	<b>Average values:</b>	<b>15.2 MPa</b>
	<b>Standard deviation</b>	<b>±1.9 MPa</b>

The typical failure pattern is illustrated in Figure 2b. During the tests, material softening and a drop in the stress-strain curve were observed. Additionally, the dispersion of the results, attributed to material anisotropy and heterogeneity, was quantified, yielding a standard deviation of  $\pm 1.9$  MPa (12.6%).

The compressive strength and maximum force values obtained for all tested specimens are detailed in Table 4.

All results obtained from the experimental compression tests are presented in Figure 3. The average curve shown above serves as a basis for the calibration of the material model in the next sections. A critical factor in the compression tests is the friction effect that occurs between the testing apparatus and the specimen [16,17]. Additionally, the shape of the sample influences the stress-strain curve. A comparison of the strengths obtained from cubic and cylindrical samples reveals that the compressive strength of cubic samples is approximately 15% higher, a trend commonly observed in typical concrete [15]. As a result, the actual material behavior is somewhat weaker than what was measured in the current tests [16,17]. This phenomenon is well-documented in the international literature, primarily for ductile materials [17], but it also applies to brittle materials [16].

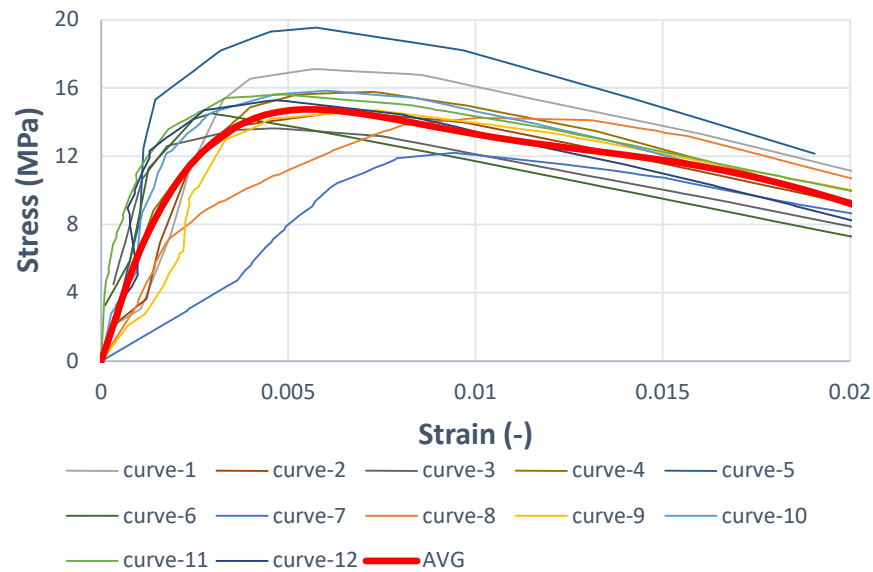


**Figure 3.** Stress-strain curves for compression of the silicate (experiments).

### 2.2. The Three-Point Bending Test Description to Estimate the Silicate Strength

The same experimental setup (Instron machine) was employed to evaluate the bending capacity of the silicate beam using the three-point bending (TPB) method. This approach ultimately allows for the estimation of the tensile strength of the silicate material, denoted as  $f_t$ . The maximum bending forces recorded for all tests are summarized in Table 5, while a typical failure pattern is shown in Figure 4b, corresponding to the initial test configuration illustrated and discussed in Figure 4a.

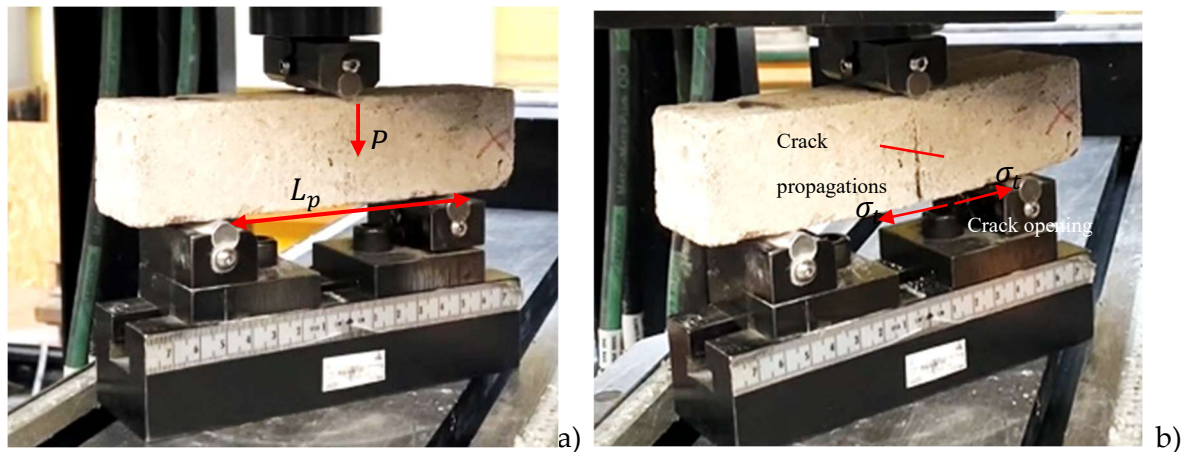


**Figure 4.** Experimental TPB test; a) sample before the test; b) sample after the test with visible fracture mechanism.

**Table 5.** The bending capacity.

No. sample	Maximum bending force (N) – $P$	Maximum tensile stress due to bending (MPa) – $\sigma_t$
1	1150	2.69
2	1290	3.01
3	1450	3.41
4	1350	3.16
5	1090	2.55

6	1400	3.27
7	1370	3.21
8	1420	3.32
<b>Average values:</b>	<b>1315</b>	<b>3.1</b>

Given the distance between the supports ( $L_p=100$  mm) the maximum bending moment MMM was calculated using the formula  $M = P \cdot L_p/4$ , where P represents the applied load. To determine the maximum bending tensile stress  $\sigma_t$ , the maximum moment  $M$  is divided by the section strength  $i$ . For a rectangular cross-section (approximately square in this analysis), the section modulus  $i$  is given by  $W \cdot H^2/6$ , as detailed in Table 2.

In the following figure, the sample can be seen before and after loading. The failure mode occurs through crack opening, corresponding to Mode I fracture, Figure 4-b.

The average maximum bending force  $P$  recorded during the tests was 1315 N, while the average maximum tensile stress due to bending  $\sigma_t$  was calculated to be 3.1 MPa. However, the actual tensile strength  $f_t$  is expected to be lower, as reported in the literature [18,19]. A detailed analysis explaining this discrepancy will be provided in Section 3.2.

### 2.3. Description of the Perforation and Impact Test

The perforation tests demonstrated the impact resistance of the silicate material. Ballistic tests were conducted using a pneumatic gas gun that accelerates a conical projectile (Figure 5b) to reach an initial impact velocity  $V_0$  at the end of the gas gun barrel (Figure 5a). The experimental setup for the perforation tests is presented, along with the system used to fix the sample. The sample holder ensures precise centring of the impact point and prevents any slipping during the test. The projectile, with its shape and characteristics, is also shown, Figure 5-b.

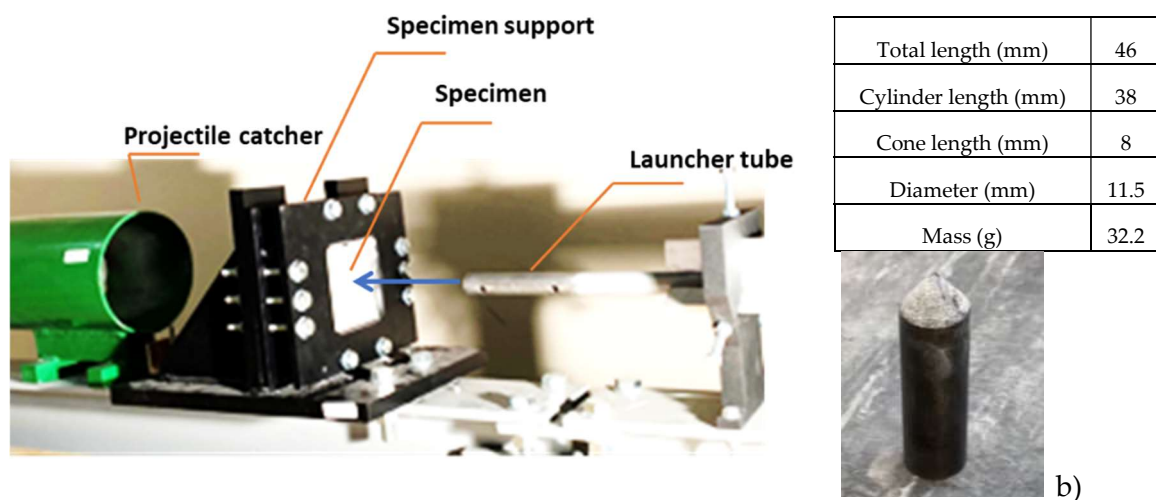


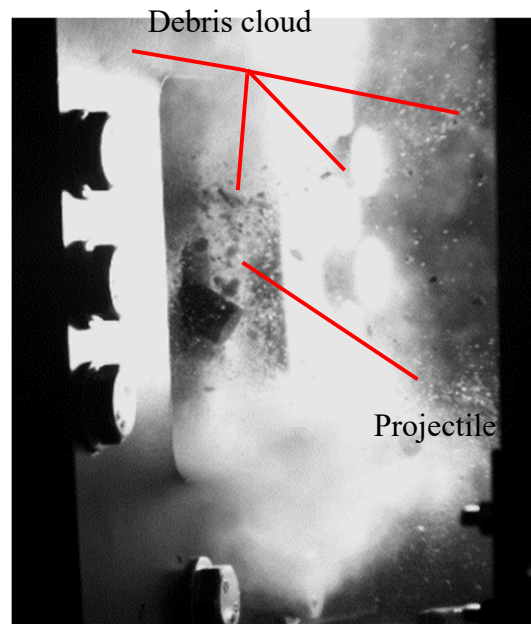
**Figure 5.** Experimental set-up for perforation of the silicate plate; a) sample fixed before the test; b) conical projectile machined with hard steel.

Different initial velocities were achieved by varying the gas pressure in the tank, with typical values provided in Table 6 for pressures ranging from 2 to 5 bars. Using these initial velocities, the kinetic energy transferred to the specimens was calculated, with values approaching or below the ballistic limit. When  $V_0$  exceeds the ballistic limit  $V_B$ , the projectile perforates the silicate plate, as observed in one of the tests.

**Table 6.** The shooting parameters of the gas gun.

Gas gun pressure (bar)	Initial impact velocity (m/s)	Projectile kinetic Energy (J)
2	44.0	31.2
3	67.0	72.3
5	88.0	124.7

In one test, the projectile successfully perforated the sample at an initial velocity of 88 m/s, as shown in Figure 6. All detailed data and key results from the perforation tests are presented in Table 7, with additional information provided in Appendix A. Notably, perforation of the silicate specimen occurred in 2 out of 3 tests when the maximum impact velocity was applied, as seen in Table 7.

**Figure 6.** Recorded perforation of sample no. 1 (front view) for initial velocity 88 m/s.**Table 7.** Failure pattern description for all tests.

No. sample	Initial velocity (m/s)	Front hole diameter (mm)	Front hole deep (mm)	Back hole diameter (mm)
1	88	18.0	exit hole (perforation)	83.0
2	67	8.5	8.2 (reflection)	86.0
3	44	5.8	4.0 (reflection)	lack
4	88	19.0	exit hole (reflection)	84.0
5	67	8.9	7.6 (reflection)	62.0
6	44	9.5	3.6 (reflection)	lack
7	88	21.0	exit hole (perforation)	89.0

During test no. 4, the projectile was deflected at an initial velocity of 88 m/s (Figure 7). A residual velocity sensor, typically based on laser and mirrors as described in [20] for metal plates, was not used in this study due to the excessive amount of debris, which interfered with measurements.

Instead, all tests were recorded using a high-speed camera with a time resolution of 20  $\mu$ s, capturing both the front and back sides of the silicate plate.

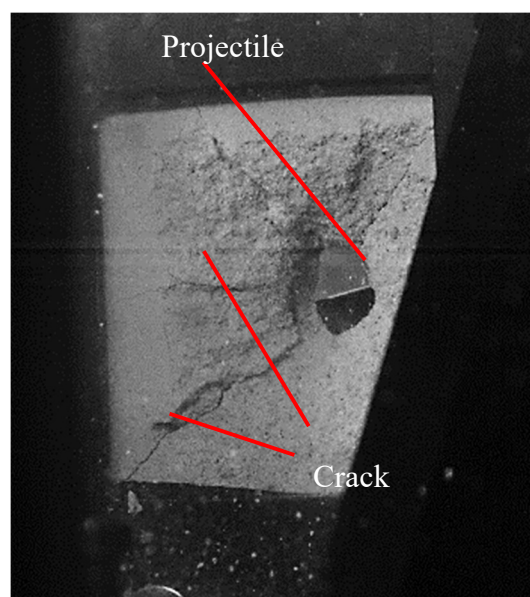


**Figure 7.** Frame during test no. 4 (the reflection of the projectile is visible—back view) for initial velocity 88 m/s.

At the lowest initial impact velocity,  $V_0 = 44$  m/s (tests no. 3 and 6), no observable spalling was found on the back side, with only faint cracks visible. Consequently, no back hole diameter was observed. A small crater appeared on the front side, with a depth of 4 mm and a diameter of 5.8 mm in test no. 3, and 3.6 mm in depth and 9.5 mm in diameter in test no. 6. For the mid-range impact velocity of 67 m/s, perforation was incomplete. On the back side, the spalling diameters were 86 mm and 62 mm for tests no. 2 and 5, respectively. On the front side, a small crater with faintly visible cracks was observed, with diameters of 8.5 mm and 8.9 mm, and depths of 8.2 mm and 7.6 mm, respectively. At the highest impact velocity tested, 88 m/s, spalling diameters of 83 mm, 84 mm, and 89 mm were produced in tests no. 1, 4, and 7, respectively. However, in test no. 4, the projectile failed to perforate the plate, instead rebounding and landing in front of the plate, as shown in Figure 7. Craters with exit holes were visible, with front side diameters of 18 mm, 19 mm, and 21 mm for tests no. 1, 4, and 7, respectively.

### 3. Numerical Simulations, Modeling of the Behavior, Damage and Failure

The Abaqus/Explicit software was employed to simulate all previously described experimental tests on the silicate blocks. In the simulations, silicate blocks were discretized using C3D8R solid finite elements. The Concrete Damage Plasticity (CDP) model was applied to represent the behaviour of the silicate specimens, while other components such as the compression plates, bending cylinders, and projectile used in the perforation test were assumed to be rigid. General contact with a friction coefficient of 0.1 was implemented, and the simulations accounted for the creation of newly eroded surfaces in regions experiencing damage and failure under significant deformation. An accurate simulation of silicate damage and failure was essential, particularly for capturing behavior at advanced deformation stages. The CDP model, which has been widely used for concrete materials [21–25], was chosen here due to silicate's mechanical similarity to concrete, including its softening behavior associated with micro-crack growth defined as “damage” in continuum mechanics. The model effectively differentiates between tension and compression behaviors, with softening predominantly occurring in the tensile zones where deformation localizes. This study applied the CDP model, as detailed in references [21–25]. The model integrates isotropic damaged elasticity with both tensile and compressive plasticity, capturing concrete-like irreversible behavior. It combines nonassociated multi-hardening plasticity and scalar (isotropic) damaged elasticity to model the

progressive damage associated with fracture, allowing for element deletion based on material failure criteria. In the initial state, the CDP model [22,24,25] assumes isotropic elasticity for silicate, as specified in Appendix B (\*Elastic keyword). As deformation progresses, the Cauchy stress tensor  $\underline{\sigma}$ , is defined relative to the effective stress tensor  $\underline{\bar{\sigma}}$ , as follows:

$$\underline{\sigma} = (1 - d) \underline{\bar{\sigma}}, \quad (1)$$

where  $d$  is a scalar damage variable ( $0 \leq d \leq 1$ ). The model uses typical additive strain rate decomposition, which is valid for small elastic strain:

$$\underline{\dot{\epsilon}} = \underline{\dot{\epsilon}}^{el} + \underline{\dot{\epsilon}}^{pl}, \quad (2)$$

where  $\underline{\dot{\epsilon}}$  is total strain rate tensor,  $\underline{\dot{\epsilon}}^{el}$  is elastic and  $\underline{\dot{\epsilon}}^{pl}$  is plastic part of the strain rate tensor. The effective stress tensor  $\underline{\bar{\sigma}}$  is related to the strain difference  $\underline{\epsilon} - \underline{\epsilon}^{pl}$ :

$$\underline{\bar{\sigma}} = D_0^{el} (\underline{\epsilon} - \underline{\epsilon}^{pl}), \quad (3)$$

where  $D_0^{el}$  is initial undamaged elastic stiffness of the material. The degraded elastic stiffness  $D^{el}$  is equal to  $(1 - d) D_0^{el}$ . The evolution of the scalar damage variable  $d$  is the following:

$$d = d(\underline{\bar{\sigma}}, \underline{\bar{\epsilon}}^{pl}), \quad (4)$$

where  $\underline{\bar{\epsilon}}^{pl}$  is a set of strain hardening (softening) variables:

$$\underline{\bar{\epsilon}}^{pl} = \begin{bmatrix} \underline{\bar{\epsilon}}_t^{pl} \\ \underline{\bar{\epsilon}}_c^{pl} \end{bmatrix} \text{ and } \dot{\underline{\bar{\epsilon}}}^{pl} = h(\underline{\bar{\sigma}}, \underline{\bar{\epsilon}}^{pl}) \cdot \underline{\dot{\epsilon}}^{pl}. \quad (5)$$

The strain hardening and softening of the material in compression and in tension are calibrated based on the uniaxial compressive test (point 2.1) and based on the tripoint bending test (point 2.2). The initial stiffness of the material is calculated based on average stress-strain curve, see Figure 3. All the material parameters used in the simulations are presented in Appendix B.

The emergence of microcracks and concrete crushing is indicated by the progressive evolution of the hardening variables. These variables govern the development of the yield surface  $F(\underline{\bar{\sigma}}, \underline{\bar{\epsilon}}^{pl})$  and the degradation of the elastic stiffness. Additionally, they are closely connected to the dissipated fracture energy necessary for the initiation of microcracks. The yield function,  $F(\underline{\bar{\sigma}}, \underline{\bar{\epsilon}}^{pl}) \leq 0$ , defines a surface within the effective stress space, and it plays a critical role in determining failure or damage states. The yield function proposed by Lubliner et al.[24] is used in CDP model, as follows:

$$F(\underline{\bar{\sigma}}, \underline{\bar{\epsilon}}^{pl}) = \frac{1}{1 - \alpha} (\bar{q} - 3\alpha\bar{p} + \beta(\underline{\bar{\epsilon}}^{pl}) \langle \bar{\sigma}_{max} \rangle - \gamma \langle -\bar{\sigma}_{max} \rangle) - \bar{\sigma}_c(\underline{\bar{\epsilon}}_c^{pl}) \leq 0. \quad (6)$$

The procedures of the parameters  $\alpha$ ,  $\gamma$  and function  $\beta(\underline{\bar{\epsilon}}^{pl})$  identification are explained in [22]. The variables  $\bar{p}$ ,  $\bar{q}$  and  $\bar{\sigma}_{max}$  are effective hydrostatic pressure, Mises equivalent effective stress and maximum effective stress. The Macauley bracket  $\langle \cdot \rangle$  in previous formula makes  $\gamma$  parameter meaningful only in triaxial compression state of stress if  $\bar{\sigma}_{max} \geq 0$  in meridian plane. The biaxial compression strength effects the parameter  $\alpha$ . The function  $\bar{\sigma}_c(\underline{\bar{\epsilon}}_c^{pl})$  describes the uniaxial compressive behaviour (see keyword \*Concrete Compression Hardening). In CDP model nonassociated plastic flow rule is used, as follows:

$$\underline{\dot{\epsilon}}^{pl} = \lambda \frac{\partial G(\underline{\bar{\sigma}})}{\partial \underline{\bar{\sigma}}}, \quad (7)$$

where:

$$G = \sqrt{(\epsilon \sigma_{t0} \tan \psi)^2 + \bar{q}^2} - \bar{p} \tan \psi. \quad (8)$$

In the previous relation, Equation (8),  $\psi$  is the dilation angle in the meridian plane  $\bar{p} - \bar{q}$  for high triaxial compression and  $\sigma_{t0}$  is uniaxial tensile stress at failure.  $\epsilon$  is the eccentricity of the plastic flow potential. The further research should be focused on the experimental test in advanced state of stress however only the compressive and tensile zone were investigated in this research (compression and 3-point bending test). The parameters which of the yield function  $F$  and of the plastic potential  $G$  in the simulations are defined in appendix B (see keyword \*Concrete Damaged Plasticity). In the present paper the typical values of these four parameters for concrete are assumed due to the lack of the triaxial test of the silicate. To clarify the effect of these parameters the loading function  $F$  is presented in Figure 8 in plane stress and in meridian plane. Based on the presented in Sections 2.1 and 2.2 tests the evolution of the internal variables like equivalent plastic strain and

damage variables in tension and in compression are performed. In CDP the fracture energy regularization of the material model in tensile zone is used. The softening part of the stress-strain curve in tension is represented in the model by the stress-displacement curve. The linear relation is used in the approximation (see keyword \*Concrete Tension Stiffening). The appropriate damage curves in compression and tension are also presented (see keywords \*Concrete Compression Damage and \*Concrete Tension Damage in Appendix B).

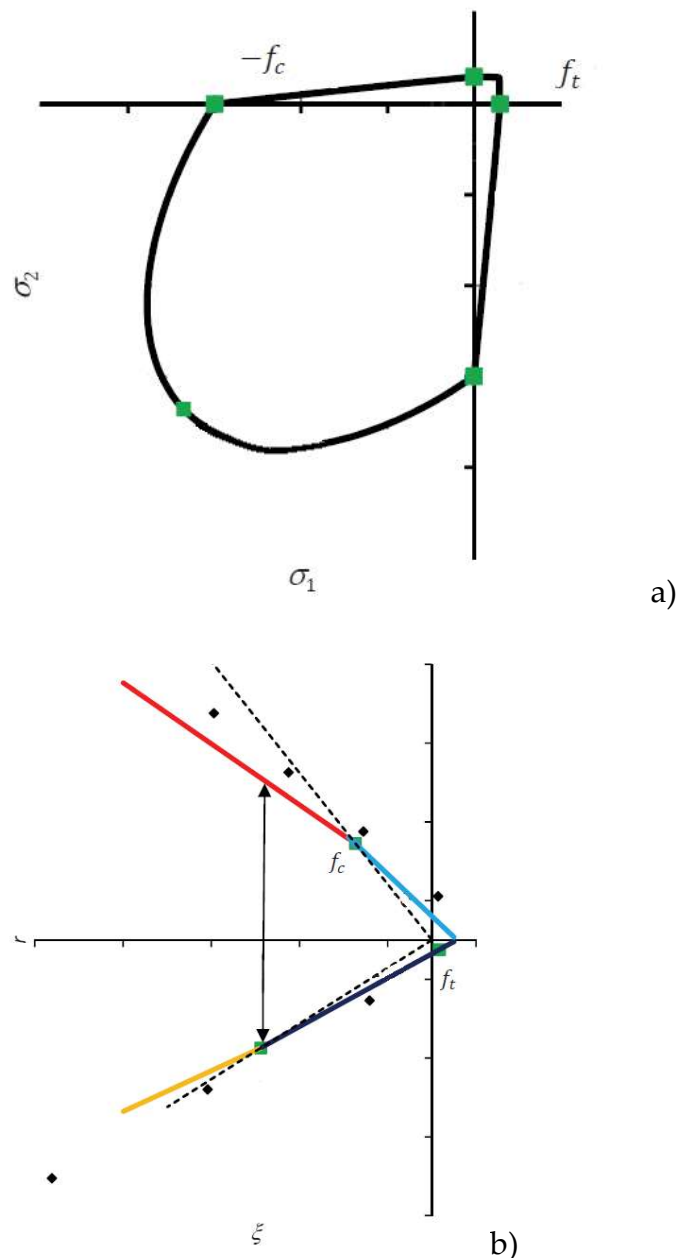


**Figure 8.** The loading function  $F$  in: a) plane stress condition and b) meridian plane [22].

In summary, the CDP model in Abaqus incorporates three main considerations for modelling the behavior of silicate material: (1) an asymmetry in yield strength between tension and compression, (2) an initial phase of hardening followed by softening under compressive loads, alongside purely softening behavior under tensile loads, and (3) differential degradation of elastic stiffness in tension versus compression. For all simulations, a consistent mesh discretization was applied with a characteristic finite element length of 2 mm to ensure uniform accuracy across analyses. The authors check the effect of the mesh size on the numerical results and the pathological mesh size dependency was not observed due to regularisation. The subsequent sections present the

principal results from the numerical simulations for compression, tension, and perforation, each compared with the experimental outcomes to validate the model accuracy.

### 3.1. Compression Test of Silicate, Comparison Between Experiments and Modeling

The stress-strain curves derived from numerical simulations were compared to those recorded during experimental testing, as illustrated in Figure 9. These curves show a good agreement, indicating that the simulation accurately reflects the material behavior under compressive load. The simulation results demonstrate the expected response characteristics of the silicate material, including the initial elastic region, the yield point, and subsequent softening behavior. This agreement confirms the accuracy of the CDP model in representing the progressive material damage and failure modes observed experimentally.

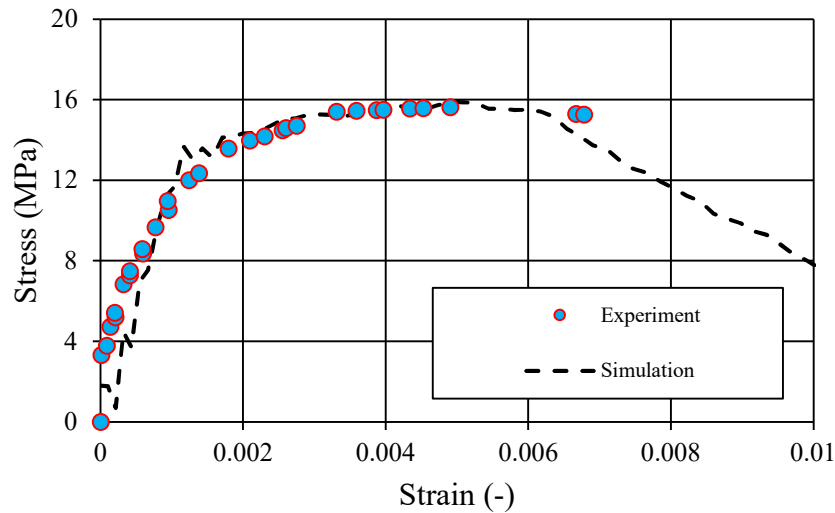


**Figure 9.** Comparison of Stress-Strain Curves in compression: Experimental Data vs. Simulation.

Additionally, the failure pattern observed in the simulations, described in Figure 10, is similar to the one observed during experiments, showing a similar shear-dominant damage mechanism and crack propagation pattern. The development of shear bands and the gradual coalescence of micro-cracks into primary failure planes can be seen both in the simulated and experimental results. This shear-dominated failure is typical for brittle materials under compressive loading, where localized shear zones precede the ultimate collapse. Moreover, the model prediction of post-failure behavior captures the subtle changes in stress redistribution within the material, further supporting its validity. This agreement between the simulated and experimental failure patterns suggests the CDP model robustness in capturing not only peak strength but also the softening and residual stress response of the silicate material under load.

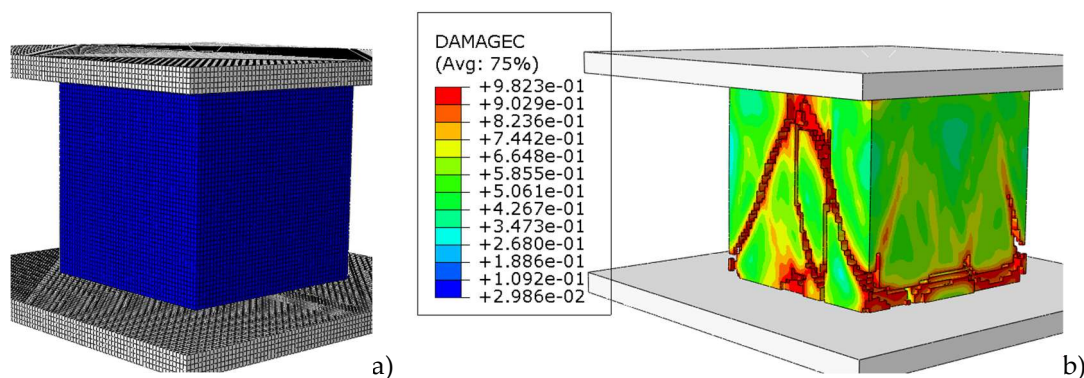


**Figure 10.** Numerical model; a) sample before the test (mesh); b) sample after the test with visible fracture mechanism.

### 3.2. Three-Point Bending Test, Comparison Between Experiments and Simulations

The force-displacement curves for three numerical cases, each with a different assigned tensile strength ( $f_t$  equal to 0.75 MPa, 1.05 MPa and 1.25 MPa), are displayed in Figure 11a. For comparison, the experimentally obtained average maximum force value is also presented in the same figure. The curves reveal how variations in tensile strength impact the force-displacement response of the silicate material, providing insights into the model's sensitivity to tensile strength adjustments. In Figure 11b, the relationship between tensile strength  $f_t$  and bending strength  $\sigma_t$  is shown as a linear trend, with a slope value of  $\alpha$  equal to 0.334, which is applied as a correction factor to refine the model's tensile strength parameters. This linear correlation indicates that as tensile strength increases, the corresponding bending strength follows predictably, supporting the use of this slope as a reliable scaling factor. The established correction factor enables an accurate calibration of tensile strength within the model, enhancing its predictive capabilities under bending conditions. Additionally, the use of notched silicate specimens subjected to three-point bending tests is noted, as these configurations are occasionally employed to study fracture mechanics in brittle materials.

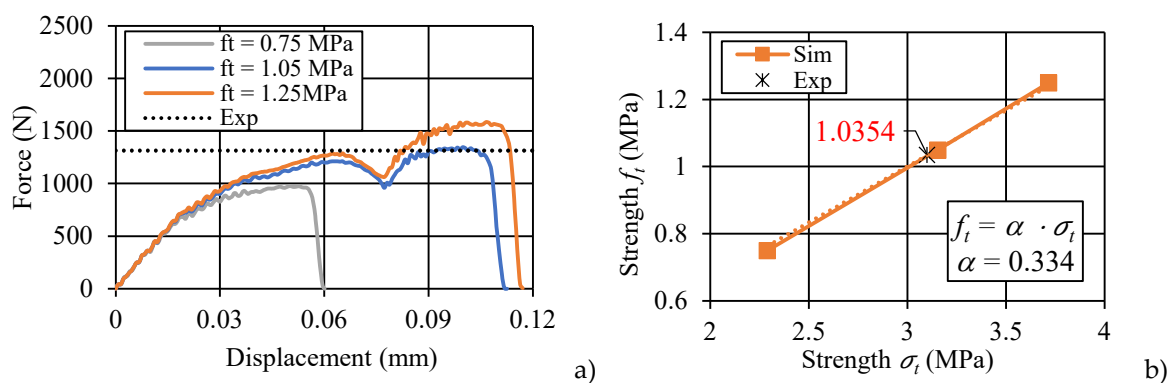


**Figure 11.** Numerical analysis results; a) force-displacement curve; b) strength  $f_t$  versus strength  $\sigma_t$  trend (calibration with experiment).

In such cases, crack initiation and propagation generally occur along the vertical axis, corresponding to the direction of maximum tensile stress, as observed in previous studies [21]. This calibrated model, with adjusted tensile properties, is expected to accurately capture the initiation and progression of fractures, especially in scenarios involving tensile and bending stress distributions, Figure 12.

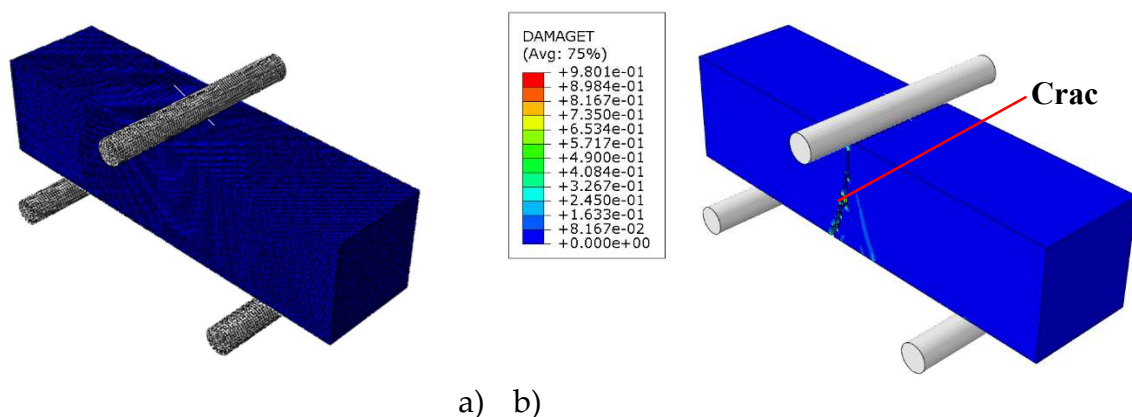


**Figure 12.** Numerical model results; a) sample before the test; b) sample after the test with visible fracture mechanism.

The calibration process outlined indicates that the tensile strength of the silicate material  $f_t$  has been determined to be 1.05 MPa. This calibrated value plays a crucial role in the accuracy of numerical simulations related to both compression and perforation tests. By incorporating this tensile strength

into the numerical models, it is ensured that the material response to loading conditions reflects realistic behavior, thereby able to predict validities of the simulations. In the context of the compression tests, the calibrated tensile strength is essential for understanding the interplay between tensile and compressive stresses during loading. Similarly, for the perforation tests, accurate tensile strength values are important for modeling the material resistance to impact and penetration, which can significantly influence the failure mechanisms observed during experiments.

### 3.3. Perforation Tests, Validation of the Numerical Model, Comparison Between Experiments and Simulations

The numerical model for perforation is defined by a silicate plate represented with the Concrete Damage Plasticity (CDP) material model, while the projectile is assumed to be a rigid body. The fixation systems consist of two square rigid frames that secure the plates in place. The perforation models are developed based on the experimental configurations detailed in Section 2.3. Three initial impact velocities were considered in the simulations. The failure patterns observed during the tests are summarized in Table 8. Key parameters, including the front hole diameters, front hole depths, and back hole diameters, were compared between experimental and numerical results. The numerical and experimental data show a strong agreement. The projectile successfully perforated the silicate plate only at an initial impact velocity of 88 m/s, while the ballistic limit was estimated to be approximately 67 m/s.

**Table 8.** Failure pattern description for all simulations versus experiments.

Initial velocity (m/s)	Front hole diameter (mm)		Front hole deep (mm)		Back hole diameter (mm)	
	Experiment	Simulation	Experiment	Simulation	Experiment	Simulation
88	19.3	20	exit hole (perforation)	exit hole (perforation)	85.3	88.0
67	8.7	12	7.9 (reflection)	9 (reflection)	74.0	60.0
44	7.7	10	3.8 (reflection)	6 (reflection)	lack	lack

Similar observations were noted in the numerical simulations, as illustrated in Table 8 and Figure 13. The damage and failure patterns for all three impact simulations (with initial velocities of 44 m/s, 67 m/s, and 88 m/s) agree with those observed during experimental tests, both in front and back views. This consistency between experimental and numerical reinforces the validity of the numerical model in predicting the behavior of silicate materials under perforation conditions.

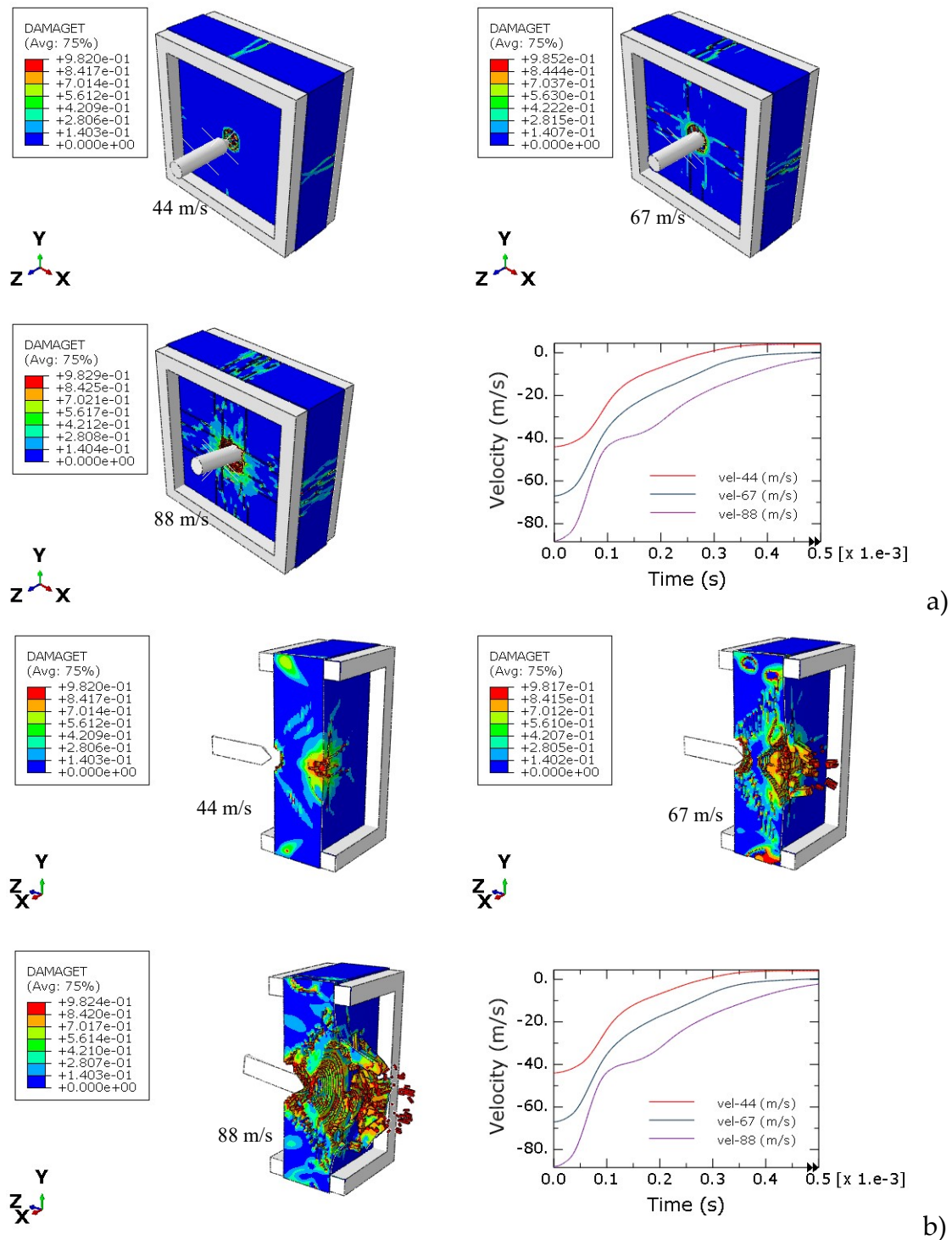


**Figure 13.** Perforation numerical results for initial velocities 44 m/s, 67 m/s and 88 m/s; a) front view; b) back view with cut plane.

Numerical simulations were employed to define the projectile velocity over time, as illustrated in Figures 13a and 13b. The projectile experiences deceleration upon contact with the silicate plate. Notably, perforation of the plate occurs only at the maximum impact velocity. The spalling failure mode, characterized by a cup-cone formation, is observed in the simulations, mirroring the behavior seen during the experimental tests. Furthermore, the extent of damage to the silicate material is directly influenced by the initial impact velocity of the projectile, indicating a clear correlation between impact velocity and the resulting failure mechanisms.

#### 4. Conclusions

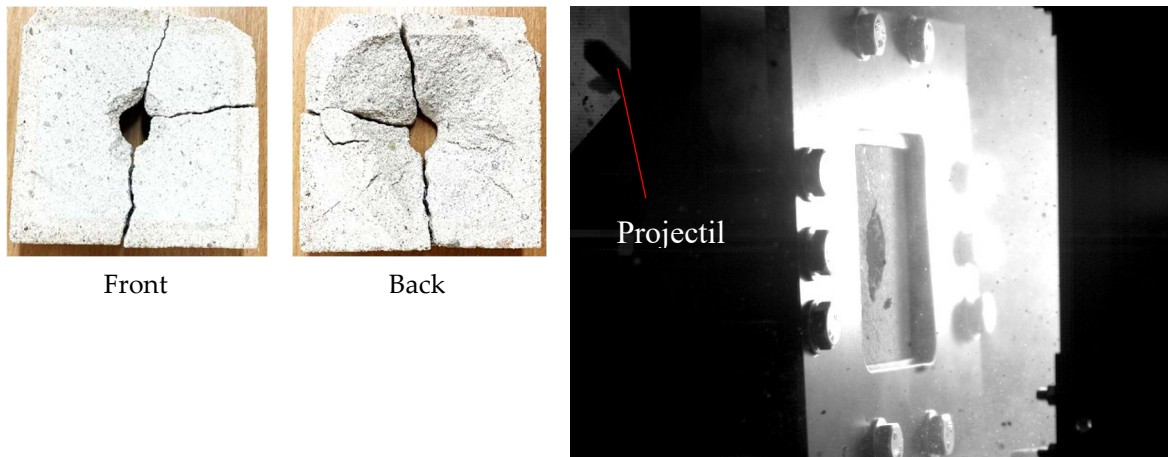
The present study investigated the behavior of silicate material under both static and dynamic loading conditions. Experimental compression tests were conducted on cubic samples, while the tensile strength of the silicate was evaluated through three-point bending tests. Additionally, the resistance of silicate to dynamic impacts with a rigid projectile at velocities near the ballistic limit was assessed. The experimental findings facilitated the calibration of a numerical model that is commonly employed to simulate the behavior of brittle materials. A critical aspect of accurately representing the experimentally observed behavior in numerical simulations was the selection of the appropriate material model. In this work, the Concrete Damage Plasticity (CDP) model was used for all simulations. This model is particularly suitable for brittle materials, as it effectively captures the non-linear and asymmetric responses typical of such materials under varying stress states. The computational analyses encompassed all three types of experiments: compression, three-point bending, and perforation. The results obtained from the numerical simulations were in correct agreement with the experiments, both quantitatively and qualitatively, demonstrating the robustness of the CDP model in representing the mechanical behavior of silicate. The most significant contributions of this study to the understanding of brittle materials are as follows:

- **Original loading tests for various strain rates and loading paths:** The research incorporated a comprehensive range of loading scenarios, including compression, three-point bending, and impact tests. This variety is instrumental for the calibration of analytical models, providing a more nuanced understanding of material behavior under different loading conditions.
- **Calibration of the numerical model for the analyzed silicate:** The successful calibration of the CDP model specifically for silicate enables more accurate predictions of material performance in practical applications, which is essential for engineering and structural design.
- **Conducting numerical simulations of all experimental tests:** The integration of numerical simulations with experimental data allows for a thorough validation of the model. By considering the material behavior and boundary conditions, the study reinforces the reliability of the model.
- **Validation of the model through comparative analysis:** The validation process, which involved comparing numerical results with experimental data, provides confidence in the model's applicability for future studies and practical implementations. This aspect is crucial for advancing the understanding of brittle materials and optimizing their use in structural applications.

Therefore, this research not only enhances the understanding of silicate materials under various loading conditions but also establishes a reliable numerical framework for predicting their behavior, thereby contributing to the broader field of material science and engineering.

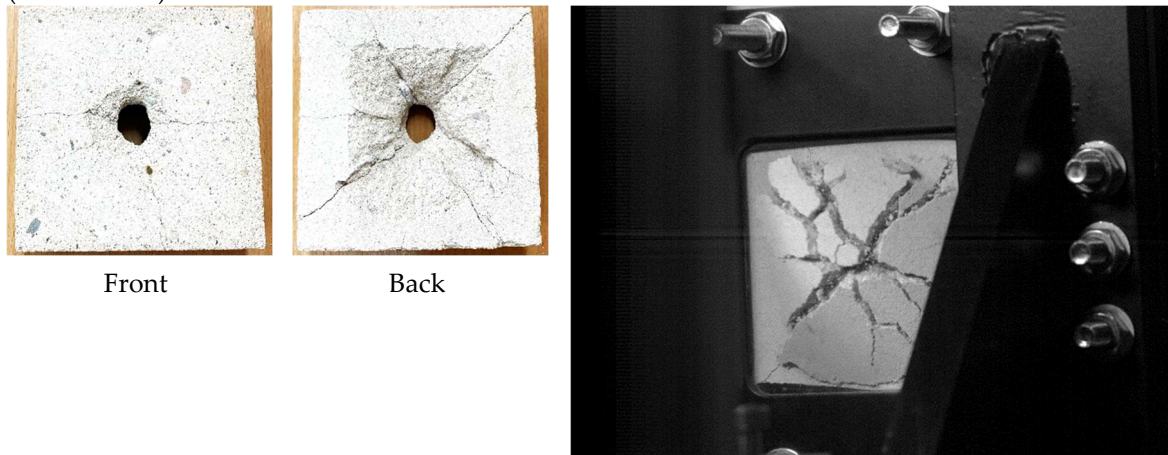
#### Appendix A

The following failure mechanisms in perforation tests are obtained. All data compatible with Table 7 for the maximal velocity are presented in Table A1. The same information for the middle velocity is presented in Table A2 but for the lowest impact velocities in Table A3.

**Table A1.** Perforation results for initial velocity 88 m/s.

**Test no. 1** (shooting pressure 5 bars, initial velocities 88 m/s)

The cracks open after removing the plate from the support system. The both side views are presented and the frame from the recording with a visible hole and projectile after perforation (which turns)



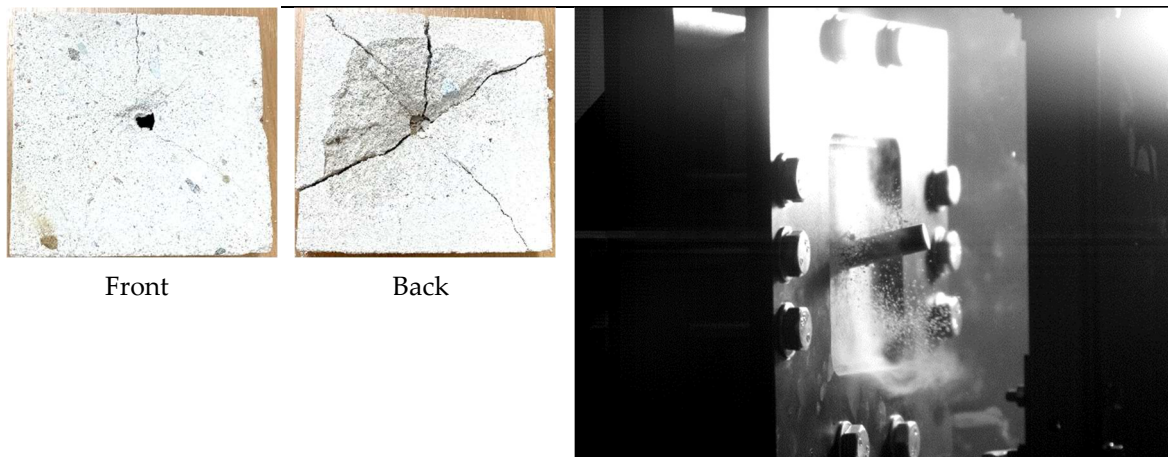
**Test no. 4** (shooting pressure 5 bars, initial velocities 88 m/s)

The cracks are not visible on the front side. The both side views are presented and the frame from the recording with visible spalling



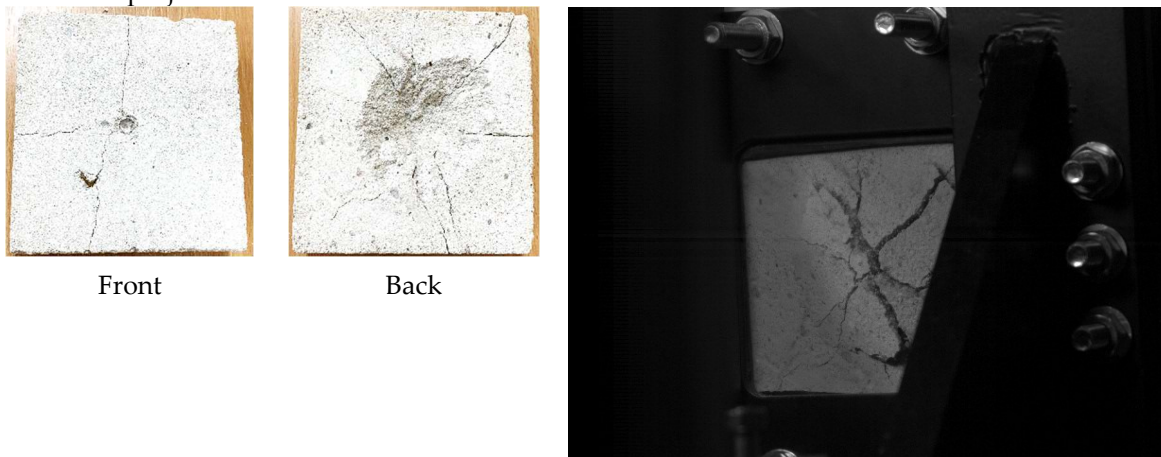
**Test no. 7** (shooting pressure 5 bars, initial velocities 88 m/s)

The cracks on the front side open during impact. The both side views are presented and the frame from the recording with visible hole and projectile which perforate the plate.

**Table A2.** Perforation results for initial velocity 67 m/s.

**Test no. 2** (shooting pressure 3 bars, initial velocities 67 m/s)

The cracks are barely visible on the front side and it opens after removing the plate from the support system. The both side views are presented and the frame from the recording with a visible crater and projectile



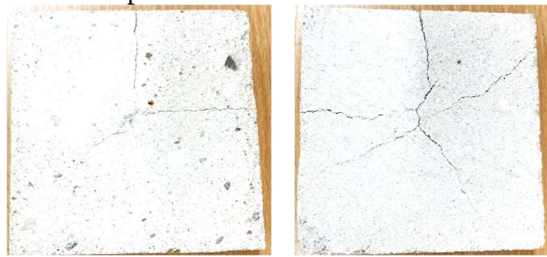
**Test no. 5** (shooting pressure 3 bars, initial velocities 67 m/s)

The cracks are barely visible on the front side. The both side views are presented and the frame from the recording with a visible spalling

**Table A3.** Perforation results for initial velocity 44 m/s.

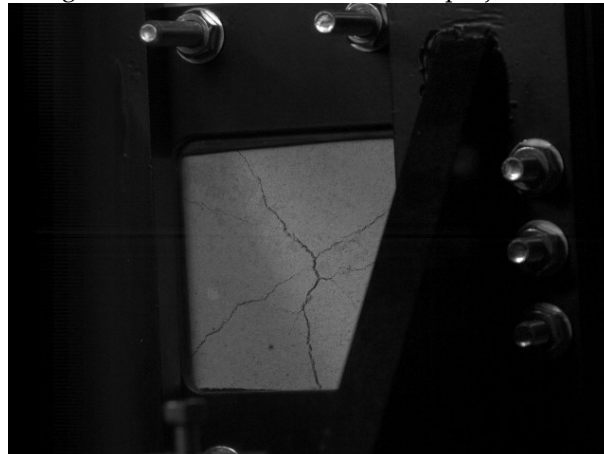
**Test no. 3** (shooting pressure 2 bars, initial velocities 44 m/s)

The cracks are not visible on the front side and are barely visible on the end side. The both side views are presented and the frame from the recording with a small visible crater and projectile



Front

Back



**Test no. 6** (shooting pressure 2 bars, initial velocities 44 m/s)

The cracks are not visible on the front side and are barely visible on the end side. The both side views are presented and the frame from the recording with a visible cracks during impact.

## Appendix B

The complete definition of the silicate material used in presented simulations is in Table A4.

**Table A4.** Material definition (CDP model in SI units).

*Density		*Concrete Tension Stiffening, type=displacement
1600,		1.25e6, 0.
*Elastic		0.0125e6, 0.15e-3
5.2e9, 0.2		*Concrete Tension Damage, type=displacement
*Concrete Damaged Plasticity		0., 0.
36., 0.1, 1.15, 0.666		0.99, 0.15e-3
*Concrete Compression Hardening		*Concrete Failure, type=displacement
11.906e6, 0.		,, 0.98,
12.385e6, 0.00039		
12.859e6, 0.0008697		
13.333e6, 0.0014491		
14.255e6, 0.0032456		
14.574e6, 0.0051084		
8.19e6, 0.1		
*Concrete Compression Damage		
0., 0.		
0., 0.00039		
0., 0.0008697		
0., 0.0014491		
0., 0.0032456		
0., 0.0051084		
0.43804, 0.1		

## References

1. Tu Y. Shi P. Liu D. Wen R. Yu Q. Sascd G. Elfgren L. Mechanical properties of calcium silicate hydrate under uniaxial and biaxial strain conditions: a molecular dynamics study. *Physical Chemistry Chemical Physics*. 2022;24:1156-1166. <https://doi.org/10.1039/D1CP04474E>
2. Jasiński R. Drobiec Ł. Piekarczyk A. Mechanical Properties of Masonry Walls Made of Calcium Silicate Materials Made in Poland. Part 1. Masonry Properties and Compressive Strength. *Procedia Engineering*. 2016. 161:904-910. <https://doi.org/10.1016/j.proeng.2016.08.755>
3. Jasiński R. Drobiec Ł. Piekarczyk A. Mechanical Properties of Masonry Walls Made of Calcium Silicate Materials Made in Poland. Part 2. Shear and Flexural Strength. *Procedia Engineering*. 2016. 161:911-917. <https://doi.org/10.1016/j.proeng.2016.08.756>
4. Jonaitis B. Marčiukaitis G. Valivonis J. Analysis of the shear and flexural behaviour of masonry with hollow calcium silicate blocks. *Engineering Structures*. 2009. 31(4):827-833. <https://doi.org/10.1016/j.engstruct.2009.01.001>
5. Drobiec Ł. FEM Model of the Masonry Made of Hollow Calcium Silicate Units. *Procedia Engineering*. 2017. 193:462-469. <https://doi.org/10.1016/j.proeng.2017.06.238>
6. Ferretti D. Michelini E. Rosati G. Mechanical characterization of autoclaved aerated concrete masonry subjected to in-plane loading: Experimental investigation and FE modeling. *Construction and Building Materials*. 2015. 98: 353-365. <https://doi.org/10.1016/j.conbuildmat.2015.08.121>
7. Zavalis R. Jonaitis B. Lourenço P.B. Experimental investigation of the bed joint influence on mechanical properties of hollow calcium silicate block masonry. *Materials and Structures* 2018. 51(85). <https://doi.org/10.1617/s11527-018-1215-y>
8. Raj A. Borsalkia A.C. Dixit U.S. Evaluation of Mechanical Properties of Autoclaved Aerated Concrete (AAC) Block and its Masonry. *Journal of The Institution of Engineers (India): Series A*. 2020. 101:315-325. <https://doi.org/10.1007/s40030-020-00437-5>
9. Šlivinskis T. Jonaitis B. Drobiec, Ł. Assessment of bed joints behavior of calcium silicate brick masonry during execution. *Engineering Structures and Technologies*. 2016. 8(4):143-149. <https://doi.org/10.3846/2029882X.2016.1238784>
10. Marčiukaitis G, Jonaitis B, Valivonis J. Peculiarities of masonry deformation properties from hollow calcium silicate blocks. In: *Theoretical foundations of civil engineering. Polish–Ukrainian Transactions*. 2004. 910-918. Warsaw. Dnepropetrovsk. <https://doi.org/10.1080/13921525.2001.10531759>
11. EN 772-1:2000. Methods of tests for masonry units—part 1: determination of compressive strength. CEN
12. EN 1015-11:1999. Methods of tests for mortar for masonry—part 11: determination of flexure and compressive strength of hardened mortar. CEN
13. Silikaty Szlachta S.C. (2023). Retrieved from <https://silikaty-szlachta.pl/oferta-blozki-silikatowe-rozno-rozmiary> (Accessed on November 2023)
14. PN-EN 771-1+A1:2015-10. Requirements for masonry elements—Part 1: Ceramic masonry elements. Polski Komitet Normalizacyjny. 2015.
15. Ossowski J. Experimental and numerical analysis of silicate elements perforation. Master thesis. Poznan University of Technology. 2023. 1-55.
16. Bandeira V.V. La Torre K.R. Kostas L.E., Marangon E. Riera J.D. Influence of contact friction in compression tests of concrete samples. *Construction and Building Materials*. 2022. 317:125811. <https://doi.org/10.1016/j.conbuildmat.2021.125811>
17. Jankowiak T. Rusinek A. Łodygowski T. Validation of the Klepaczko-Malinowski model for friction correction and recommendations on Split Hopkinson Pressure Bar. *Finite Elements in Analysis and Design*. 2011. 47:1191–1208. <https://doi.org/10.1016/j.finel.2011.05.006>
18. Liao Z.Y. Zhu J.B. Tang C.A. Numerical investigation of rock tensile strength determined by direct tension, Brazilian and three-point bending tests. *International Journal of Rock Mechanics and Mining Sciences*. 2019. 115:21-32. <https://doi.org/10.1016/j.ijrmms.2019.01.007>
19. Efe T. Demirdag S. Tufekci K. Sengun N. Altindag R. Estimating the direct tensile strength of rocks from indirect tests. *Arabian Journal of Geosciences*. 2021. 14:1343. <https://doi.org/10.1007/s12517-021-07539-9>
20. Jankowiak T. Wykorzystanie Metod Eksperymentalnych i Symulacji Komputerowych do Określania Właściwości Materiałów Przy Dużej Prędkości Deformacji. Wydawnictwo Politechniki Poznańskiej. 2016. Poznań. Poland.
21. Kumpova I. Fila T. Vavrik D. Kersner Z. X-ray dynamic observation of the evolution of the fracture process zone in a quasi-brittle specimen. *Journal of Instrumentation*. 2015. 10(8):C08004. <https://doi.org/10.1088/1748-0221/10/08/C08004>
22. Jankowiak T. Łodygowski T. Quasi-Static Failure Criteria for Concrete. *Archives of civil engineering*. 2010. LVI(2):123-154. DOI:10.2478/v.10169-010-0007-8
23. Hillerborg A. Modeer M. Petersson P.E. Analysis of Crack Formation and Crack Growth in Concrete by Means of Fracture Mechanics and Finite Elements. *Cement and Concrete Research* 1976. 6:773–782. [https://doi.org/10.1016/0008-8846\(76\)90007-7](https://doi.org/10.1016/0008-8846(76)90007-7)

24. Lubliner J. Oliver J. Oller S. Oñate E. A Plastic-Damage Model for Concrete. *International Journal of Solids and Structures*. 1989. 25:299–329. DOI:10.1016/0020-7683(89)90050-4
25. Dassault Systemes (2017). Abaqus. Retrieve from Damaged plasticity model for concrete and other quasi-brittle materials—SIMULIA User Assistance 2023 (3ds.com) (Accessed on November 2023)

**Disclaimer/Publisher's Note:** The statements, opinions and data contained in all publications are solely those of the individual author(s) and contributor(s) and not of MDPI and/or the editor(s). MDPI and/or the editor(s) disclaim responsibility for any injury to people or property resulting from any ideas, methods, instructions or products referred to in the content.